Active membrane conductances and morphology of a collision detection neuron broaden its impedance profile and improve membrane synchrony

Running title: Impedance profile of a collision detection neuron

Richard B. Dewell[1] and Fabrizio Gabbiani[1,2]
[1]Department of Neuroscience, Baylor College of Medicine, Houston, TX, USA; [2]Department of Electrical and Computer Engineering, Rice University, Houston, TX, USA

Corresponding authors:
Fabrizio Gabbiani - gabbiani@bcm.edu
Richard B. Dewell - dewell@bcm.edu

Abstract

Our brain processes information through the coordinated efforts of billions of individual neurons, each of which transforms a small part of the overall information stream. Central to this is how neurons integrate and transform complex patterns of synaptic inputs. The neuronal membrane impedance determines the change in membrane potential in response to input currents, and therefore sets the gain and timing for synaptic integration. Using single and dual dendritic recordings *in vivo*, pharmacology, and computational modeling, we characterized the role of two active conductances g_H and g_M, meditated respectively by hyperpolarization-activated cyclic nucleotide gated (HCN) channels and by muscarine sensitive M-channels, in shaping the membrane impedance of a collision detection neuron in female *Schistocerca americana* grasshoppers. The neuron is known by its acronym LGMD, which stands for lobula giant movement detector. In contrast to other neurons where these conductances have been studied, we found that g_H and g_M promote broadband, synchronous integration over the LGMD's functional range of membrane potentials and input frequencies. Additionally, we found that the branching morphology of the LGMD helped increase both the gain and synchrony associated with the neuron's membrane impedance. The same result held for a wide range of dendritic morphologies, including those of mammalian neocortical pyramidal neurons and cerebellar Purkinje cells. Thus, these

findings further our understanding of the integration properties of individual neurons by showing the unexpected role played by two widespread active conductances and by dendritic morphology in shaping synaptic integration.

Significance Statement

Information in the brain is processed by neurons that receive thousands of synaptic inputs. Understanding how neurons integrate these inputs is critical to neuroscience. Neuronal integration depends on complex interactions of synaptic input patterns and the electrochemical properties of dendrites. Although examining the input patterns and dendritic processing *in vivo* is not yet possible in the mammalian brain, it is within simpler nervous systems. Here, we used an identified collision detection neuron in grasshoppers to examine how its morphology and membrane properties determine the gain and synchrony of synaptic integration in relation to the computations it performs. The neuronal properties examined are ubiquitous and therefore will further a general understanding of neuronal computations, including those in our own brain.

Introduction

By the nineteen forties, neuroscience had recognized that neuronal membranes exhibited bandpass impedance properties and had begun investigating which cellular mechanisms contributed to their resistance, capacitance, and inductance (Cole, 1941). The capacitance is determined by the lipid bilayer of the membrane, and its resistance by the membrane permeability, but the inductance came from an unknown source. After the discovery of active conductances, it became clear that their kinetics produced a phenomenological inductance, and that its properties could be investigated using Hodgkin and Huxley's equations (Mauro, 1961; Mauro et al., 1970). In the decades since, researchers have learned a great deal about the roles of active conductances in shaping the electrical properties of

neurons, and how neuronal bandpass properties can generate rhythmic activity across neural networks (Hutcheon and Yarom, 2000; Wang, 2010; Das et al., 2017). Rhythmic activity within the brain contributes to multiple cognitive processes and to timing control across brain regions (Wang, 2010; Buzsáki and Moser, 2013).

Several membrane channels, including HCN and M channels, influence neural oscillations and synchrony both at the cellular and network level. M channels contribute to theta resonance (4-10 Hz) in pyramidal neurons (Hu et al., 2002, 2009; Hönigsperger et al., 2015), and influence network oscillations *in vivo* (Peters et al., 2005). HCN channels produce theta resonance in many neuron types (Ströhmann et al., 1995; Hutcheon et al., 1996; Hu et al., 2002; Gastrein et al., 2011), but can also generate delta resonance (1-3 Hz; Ulrich, 2014), or no resonance at all (Anderson et al., 2011). In addition to rectifying conductances like g_H and g_M, amplifying conductances such as those mediated by persistent sodium and voltage-gated calcium channels also shape the impedance profile (Hutcheon et al., 1996; Lampl and Yarom, 1997).

Another factor shaping the impedance profile of a neuron is its dendritic morphology. An extended morphology causes dendrites to be more compartmentalized which increases attenuation and phase lag of descending inputs, but simultaneously improves local coincidence detection and nonlinear processing (Häusser and Mel, 2003; London and Hausser, 2005). It has been proposed that dendritic branching and tapering optimizes integration by increasing synaptic homogeneity (Cuntz et al., 2007). Additionally, the complex dendritic morphology of pyramidal and Purkinje neurons can increase neuronal resonance (Dhupia et al., 2015; Ostojic et al., 2015). Much remains unexplored, though, on the influence that complex dendritic morphologies have on the integration properties of neurons *in vivo*.

Similarly, because the work on neuronal membrane properties has mainly been done with cultured neurons or brain slices and that the natural synaptic input patterns are still unknown for most neurons, much remains unanswered about how the impedance properties of neurons influence neural

computations. Here we used *in vivo* dendritic electrophysiology, pharmacology, and computational modeling to investigate the impedance properties of the LGMD, an identified collision detection neuron with known synaptic input patterns and dendritic computations. Experiments investigated the roles of morphology, g_H, and g_M in shaping these properties. As both g_H and g_M are sensitive to numerous modulators (Delmas and Brown, 2005; Wahl-Schott and Biel, 2009), our ability to conduct experiments *in vivo* ensures that the channels are in the relevant modulatory state. Surprisingly, the presence of these channels was found to decrease membrane resonance and oscillatory or bursting activity, instead broadening the bandpass of the neuronal membrane and increasing its consistency over different membrane potentials. Like these active conductances, the neuron's morphology also helped broaden the bandpass of the neuronal membrane and increased its synchrony.

Materials and Methods

Animals

Experiments were performed on adult female grasshoppers 7-12 weeks of age (*Schistocerca americana*). Animals were reared in a crowded laboratory colony under 12 h light/dark conditions. Animals were selected for health and size without randomization, and investigators were not blinded to experimental conditions. Sample sizes were not predetermined before experiments. The surgical procedures used have been described previously (Gabbiani and Krapp, 2006; Jones and Gabbiani, 2012; Dewell and Gabbiani, 2018a).

Visual stimuli

Visual stimuli were generated using Matlab (RRID:SCR_001622) and the Psychophysics Toolbox (PTB-3, RRID:SCR_002881) on a personal computer running Windows XP. A conventional cathode ray tube monitor refreshed at 200 frames per second was used for stimulus display (LG Electronics, Seoul, Korea). Looming stimuli are the two-dimensional projections of an object

102 approaching on a collision course with the animal. They consisted of an expanding dark square
103 simulating a solid object with half size l approaching at constant speed v (illustrated in Figure 1B). The
104 expansion profile is characterized by the ratio $l/|v|$, as previously described (Gabbiani et al., 2001).

105 **Electrophysiology**

106 Sharp-electrode LGMD intracellular recordings were carried out in current-clamp or voltage-
107 clamp mode using thin walled borosilicate glass pipettes (outer/inner diameter: 1.2/0.9 mm; WPI,
108 Sarasota, FL; see Jones and Gabbiani, 2012, as well as Dewell and Gabbiani, 2018a for details). The
109 membrane potential (V_m) and current (I_m) were low-pass filtered with cutoff frequencies of 10 kHz and
110 5 kHz, respectively. Most recordings were digitized at a sampling rate of 20,073 Hz (for some
111 experiments V_m was digitized at 40,146 Hz). We used a single electrode clamp amplifier capable of
112 operating in discontinuous mode at high switching frequencies (20-35 kHz; SEC-10, NPI, Tamm,
113 Germany). Responses to current injections were recorded in discontinuous current clamp mode (DCC).
114 For dual recordings we inserted under visual guidance a second sharp electrode into the excitatory
115 dendritic field of the LGMD (see Figure 2A) with a motorized micromanipulator (Sutter Instruments,
116 Novato, CA). Membrane potential was recorded with a second SEC-10 amplifier in bridge mode with
117 electrode resistance and capacitance compensation when not injecting current and in DCC mode while
118 injecting current. Switching frequencies, signal filtering and digitization were identical for both
119 recordings.

120 Both the physical distance along the dendrites and an estimate of the electrotonic distance
121 between recording electrode pairs were measured as follows. First, all cells were stained with Alexa
122 Fluor 594 and imaged with a CCD camera to record electrode position (Dewell and Gabbiani, 2018a).
123 Next, to estimate the dendritic distance between recording pairs, an image of the neuron and electrodes
124 (cf. Figure 2A) was imported into ImageJ (RRID:SCR_003070), the dendritic path between the
125 electrode tips was manually traced, and the corresponding path length recorded. To estimate the
126 electrotonic distance between the recording pairs we measured the amplitude of the back-propagating

action potentials (bAP) at each location and used the difference in these amplitudes. As in a previous study, the differences in bAP amplitude provided a more reliable explanatory variable for distance dependent effects (Dewell and Gabbiani, 2018a).

A neuron's frequency-dependent membrane properties are characterized by its impedance profile. The subthreshold impedance can be decomposed into input impedance which describes local change in membrane potential at the site of an input current and transfer impedance that describes change in membrane potential at remote locations after propagation through the neuron. Both input and transfer impedance shape synaptic integration within dendrites. Additionally, impedance properties at the site of spike initiation influence the transformation of membrane potential into spiking activity, including the bandpass filtering and timing of a neuron's output. If a neuron's conductance distribution is uniform, then the transfer and input impedances will have similar properties, but when it is not the impedance profile varies by location and transfer depends on the recording locations and the direction of signal propagation (Hu et al., 2009; Vaidya and Johnston, 2013).

To measure the impedance profile, we injected sine waves of increasing frequency called chirp (or zap) currents. We recorded the injected membrane current simultaneously with the membrane potential to avoid any discrepancies between the computer-generated waveform and the current injected by the amplifier. The chirp currents used were identical to those described in Dewell and Gabbiani (2018b). The chirp current is defined as $I(t) = I_p sin\phi(t)$, where $I_p$is the peak current, $\phi(t)$ is the phase of the sine wave, and its instantaneous frequency is defined as $f(t) = \frac{1}{2\pi}\frac{d\phi}{dt}$ (in units of Hz). We generally used chirps with a duration of 20 s (sometimes 30 s, as is illustrated in Figure 2B) that increased in frequency either linearly or exponentially with time. In most experiments, as well as for all simulations, we used exponentially increasing chirp currents. The linear chirp started at 0 Hz and was calculated as $I(t) = I_p \sin(\pi\beta t^2)$, with t being the time from the start of the chirp (in units of s) and β the rate of increase in instantaneous chirp frequency (in Hz/s). The exponential chirp was

151 given by $I(t) = I_p \sin(2\pi f_0 t e^{\beta t})$, where f_0 is the initial chirp frequency and β determines the
152 (accelerating) rate of frequency increase (Barrow and Wu, 2009). For all exponential chirps, we used f_0
153 = 0.05 Hz and β = 0.24 Hz which produced a chirp current increasing to 35 Hz over 20 s. We saw no
154 differences in the calculated impedance profiles with chirps having different frequency profiles, in
155 accordance with previous comparisons of impedance profiles between chirps of increasing and
156 decreasing frequencies (Ulrich 2002; Erchova et al. 2004; Hu et al. 2002; van Brederode and Berger
157 2008; van Brederode and Berger 2011) or comparison of linearly increasing chirps and sum of sine
158 wave stimuli (Hutcheon et al., 1996).

159 **Pharmacology**

160 We applied the HCN- channel blocker ZD7288 and the M-channel blocker XE991 either
161 directly in the bath saline or by local puffing as previously described (Dewell and Gabbiani, 2018a,
162 2018b). For local puffing, drugs were mixed with physiological saline containing fast green (0.5%) to
163 visually monitor the affected region and were puffed using a micropipette connected to a pneumatic
164 picopump (PV830, WPI, Saratoga, FL). For both delivery methods, drug concentrations within the
165 lobula were ~200 μM for ZD7288 and ~100-200 μM for XE991. In dual recording experiments,
166 mecamylamine was applied to block excitatory postsynaptic potentials (EPSPs) and was present in
167 both control and drug conditions. Blockade of EPSPs reduced membrane noise as well as noise in the
168 calculated impedance profiles. In paired comparisons, mecamylamine caused small increases in
169 impedance amplitude (~5%) but this difference was smaller than the variability between animals or
170 between dendritic locations. For control data we thus pooled recordings with and without
171 mecamylamine.

172 **Experimental design and statistical analyses**

173 Data analysis was carried out with custom MATLAB code (The MathWorks, Natick, MA).
174 Linear fits were done by minimization of the sum of squared errors. Before each chirp current a -2 nA
175 hyperpolarizing step current was used for monitoring the input resistance and the membrane time

constant. Unless otherwise specified, all statistical tests were made using the Wilcoxon rank sum test (WRS) which does not assume normality or equality of variance. Normality of the data was assessed by using a Lilliefors test for any tests assuming it.

The complex impedance Z was calculated as $Z(f) = \mathrm{fft}(V_m)/\mathrm{fft}(I_m)$ where fft is the (frequency dependent) fast Fourier transform, I_m the membrane current, and V_m the membrane potential. Both I_m and V_m were down sampled to 2 kHz before the fft. Z was calculated for each trial and then averaged across trials. The complex impedance is composed of the real valued resistance R and the imaginary valued reactance X: $Z = R + i\,X$. A positive reactance, or inductance, indicates that changes in V_m precede changes in I_m. Conversely, a negative reactance, or capacitance, indicates that changes in I_m precede changes in V_m. The impedance amplitude is calculated as the absolute value of Z: $|Z(f)| = \sqrt{R(f)^2 + X(f)^2}$. The impedance phase is calculated by the inverse tangent of the reactance divided by the resistance: $\Phi(f) = \tan^{-1} X(f)/R(f)$. This impedance phase is equal to the angle between the x-axis and a line from the origin to a point of the impedance locus plot (cf. Figure 4C).

Input impedance (Z_{IN}) was calculated from the V_m and I_m recorded at the site of current injection. Transfer impedance (Z_{TR}) was calculated with the I_m from the site of current injection and the V_m from the non-injected site. Voltage attenuation was calculated as the percent reduction in impedance amplitude from the current injection site to the non-injected site: $V_{att}(f) = (|Z_{\mathrm{IN}}(f)| - |Z_{TR}(f)|)/|Z_{\mathrm{IN}}(f)|$. Similarly, the phase lag was calculated as the input minus the transfer impedance phase. The phase lag was converted to a time lag by $t_{lag}(f) = \Phi(f)/(2\pi f)$ where f is the instantaneous chirp frequency (in Hz) calculated as $f(t) = \frac{1}{2\pi}\frac{d}{dt}\sin^{-1}(\frac{I(t)}{I_p})$, for details see Dewell and Gabbiani (2018b). The asynchrony was then calculated as the mean absolute time lag across frequencies.

Resonant frequency and resonance strength were calculated from the input impedance amplitude and were the frequency at which the impedance amplitude was at its maximum and the ratio

200 of the maximum impedance to the steady state impedance. Minimum and maximum phase were
201 respectively calculated as the lowest (most capacitive) and highest (most inductive) input impedance
202 phase. The impedance frequency variation was calculated as the standard deviation (across frequencies
203 ranging from 0 up to 35 Hz) of the impedance amplitude profile divided by the mean impedance
204 amplitude. Unlike resonance strength, the frequency variation statistic (f_{var}) incorporates both the
205 strength and breadth of the bandpass, giving an indication of how ohmic (or broadband) the membrane
206 is. Indeed, an ideal resistor would have a frequency variation of zero while a membrane exhibiting
207 sharp bandpass attributes would produce high frequency variation. For the membrane constant values
208 we used for our electrical circuit models (see below) f_{var} values were 18.4 for the lowpass circuit, and
209 378 for the strongest bandpass circuit. There is a potential drawback to the statistic, though, in that it
210 depends on the frequency range examined, limiting the ability to directly compare values between
211 studies examining different frequency ranges.

212 For calculating the power density of the membrane potential, we used the Matlab multitaper
213 power spectral density estimate (function 'pmtm'), with a time-half bandwidth product of 4 measured
214 over 15 octaves at frequencies of 2^{-4} to 2^{11} Hz with 8 voices (scales) per octave. All data was "zero-
215 meaned" before calculating the power density estimate and the resulting estimates were then averaged
216 across trials. For estimating the time-varying power density we used Matlab's continuous wavelet
217 transform (function 'cwt'). The frequency range was set from 0.1 to 2,000 Hz and the signal was not
218 extended. As for the spectral density estimate, wavelet transforms were calculated for individual trials
219 and the resulting wavelet transform coefficients were then averaged across trials. In the calculation of
220 both measures, the raw data was used with no down sampling or filtering.

221 **Electrical circuit model**

222 To compare LGMD membrane impedance to the impedance of an equivalent cable based on a
223 series of either RC or RLC circuits, we calculated the complex circuit impedance as follows. The RLC
224 circuit was modeled as illustrated in Figure 3F. The membrane impedance density was calculated as:

225 $$Z_m = \frac{R_m}{1 - l_{rat} + l_{rat}/(1 + i\tau_L\omega) + i\tau_m\omega}$$

226 where Z_m is input impedance density (Ωcm^2), R_m is membrane resistivity (Ωcm^2), C_m is membrane
227 capacitance (F/cm^2), τ_m (s) is membrane time constant ($\tau_m = R_m C_m$), τ_L is the inductance time constant
228 (s), ω is frequency in rad/s, l_{rat} is the ratio of the membrane conductance that is in series with the
229 inductor (range [0–1]), and $i = \sqrt{-1}$. If l_{rat} is zero, then no current will pass through the inductor and the
230 circuit is equivalent to an RC circuit with membrane impedance:

231 $$Z_m = R_m/(1 + i\tau_m\omega)$$

232 In both cases, the input impedance (Z_{IN}) was calculated by dividing Z_m by the unit surface area of the
233 cable (cm^2). We used the average dendritic circumference of our full LGMD model (20.85 μm) for the
234 cable circumference.

235 Transfer impedance measures were based upon a cable of fixed diameter and infinite length.
236 The voltage transfer along the cable was calculated as $V_{TR} = e^{-l/\lambda}$, where l (cm) is the distance
237 between the two locations and λ is the cable length constant (cm), $\lambda = \sqrt{Z_m/(R_a d b_f)}$. R_a is the axial
238 resistivity (Ωcm), d is the diameter (cm), and $b_f = 3$ is the branch factor – a scalar added to account for
239 additional attenuation due to the dendritic branching. The transfer impedance Z_{TR} at distance l from the
240 site of current injection is the product of Z_{IN} and V_{TR}.

241 **Morphological neuron models**

242 Comparisons between different cell morphologies used published neuron models downloaded
243 from ModelDB (RRID:SCR_007271). Among the available morphologies, we selected neurons
244 spanning a wide range of branching patterns and sizes. The morphologies used included a cerebellar
245 Purkinje neuron (Miyasho et al., 2001; Ostojic et al., 2015), a CA1 pyramidal neuron (Migliore et al.,
246 2004), an oriens-lacunosum/moleculare (OLM) hippocampal interneuron (Sekulić et al., 2015), and a
247 human layer 2/3 temporal cortex pyramidal neuron (Eyal et al., 2016). As we sought to compare the
248 influence of the cell morphology, all models were passive with identical membrane properties close to

249 those used in the LGMD model (C_m = 0.8 μF/cm^2, G_m = 0.1 mS/cm^2, Ra = 350 Ωcm). All simulations
250 were carried out using the NEURON software simulation package. For a passive model measuring
251 impedance with chirp currents, as was done experimentally, or with NEURON's built-in impedance
252 tools yielded the same result, so we used the built-in impedance measurement to speed up the
253 simulations carried out for Fig. 7A and B.

254 In Fig. 7G, the percentage of cell surface area with improved transfer impedance amplitude was
255 calculated from the data depicted in Fig. 7F (left). Specifically, we calculated the transfer impedance
256 amplitude between all neuron segments and compared it to the impedance amplitude of an isopotential
257 model (using the same cell morphology but with axial resistivity set to zero). The impedance amplitude
258 of an isopotential cell is $R/(1 + \omega^2\tau_m^2)^{0.5}$, where R is the membrane resistance (MΩ), ω is the frequency
259 (s^{-1}), and τ_m is the membrane time constant (s). As C_m and G_m were the same for all morphologies, their
260 membrane time constants were the same ($\tau_m = C_m G_m$) while the membrane resistance changed with
261 their total membrane area A ($R = (AG_m)^{-1}$). For each segment, we summed the surface area of all
262 segments to which a broadband signal transferred with greater gain than the isopotential value (dashed
263 line in Fig. 7F, left) and divided by the neuron's total surface area. Frequencies of 0 to 1000 Hz were
264 used and averaged with equal weight.

265 Similarly, to obtain Fig. 7H we compared the transfer impedance phase between all segment
266 pairs and compared it to the impedance phase of an isopotential equivalent. The impedance phase of an
267 isopotential cell is $\tan^{-1}(-\tau_m \omega)$, as illustrated in Fig. 7E, right. For the phase measurements, a weighted
268 average was used with the transfer amplitude between the segment pair determining the weight for
269 each frequency. As signals of some frequencies transfer better than others, the transfer phase of these
270 signals influences the membrane synchrony more. The percentage area with increased impedance
271 phase was then calculated by summing the surface area of segments with more synchronous transfer
272 phase and dividing by the total membrane surface area of the neuron. These calculations effectively
273 measure the average signal transfer of a passive cell with realistic morphology under the simplifying

assumptions that broadband inputs impinge upon the neuron with a uniform density. Although these assumptions would not necessarily hold *in vivo* where the locations and frequency of inputs is constantly changing, they provide a reasonable method of estimating transfer impedance without relying on the less realistic assumptions that all inputs impinge on a single location or that all signals only integrate at a single location, like the neuron's spike initiation zone.

Results

The LGMD (O'Shea and Williams 1974) is an identified neuron in locusts that selectively responds to visual stimuli mimicking impending collision (Schlotterer, 1977; Rind and Simmons, 1992). The LGMD possesses three dendritic fields with the largest one, field A, integrating excitatory inputs originating from every facet of the compound eye (Fig. 1A). The LGMD discriminates (simulated) approaching objects that activate thousands of facets based on the object's trajectory and spatial coherence (Fig. 1B, C; Gray et al., 2001; Dewell and Gabbiani, 2018a). The LGMD's dendritic computations and stimulus selectivity depend on the precise spatiotemporal patterning of synaptic inputs (Peron et al., 2007; Jones and Gabbiani, 2010; Zhu and Gabbiani, 2016), and their filtering by active conductances that include sodium, low voltage calcium, calcium-dependent potassium, HCN, and M channels (Gabbiani et al., 2002; Peron and Gabbiani, 2009; Dewell and Gabbiani, 2018b, 2018a). Different aspects of the LGMD's firing patterns – including burst firing – have been tied to the generation of escape behaviors (Fotowat et al., 2011; McMillan and Gray, 2015; Dewell and Gabbiani, 2018a).

The spontaneous and stimulus-evoked membrane potential spectral power density of the LGMD is highest at low frequencies. Due to the large number of synaptic inputs impinging upon the LGMD, its membrane potential exhibits a high level of spontaneous synaptic background noise that has been estimated at 2,000 synaptic inputs per second (Jones and Gabbiani, 2012). This and the short membrane time constant of the LGMD *in vivo* (~ 7 ms) raises the possibility that high frequency

298 components might dominate the LGMD's membrane potential power spectrum. Examination of the
299 membrane potential time course under constant, uniform illumination of the eye reveals both high and
300 low frequency components (Fig. 1D). After calculating the power spectral density of spontaneous
301 membrane fluctuations (see Methods), we found that 87% of the signal power was contained below 35
302 Hz with 50% at less than 7.5 Hz (Fig. 1E, black lines). This breakdown of spectral power frequencies
303 was measured under constant illumination, though, and the LGMD's principal role is detecting
304 looming stimuli.

305 During the course of looming stimuli, the number of activated ommatidia increases from ~10 to
306 over 2,500. According to the most recent estimates of LGMD excitatory contacts per ommatidium
307 (Rind et al., 2016), such stimuli would produce an increase in activated synapses from ~100 to over
308 20,000. This increased synaptic input occurs in ever tighter time windows (Fig. 1C) and might lead to a
309 corresponding shift in power towards higher frequencies. However, during looming stimuli the low
310 frequency power increased, with over 50% of it below 1.5 Hz (Fig. 1E, blue lines). As most of the
311 membrane depolarization and spiking activity generated by looming occurs shortly before the time of
312 collision, we used wavelet analysis to resolve the frequency content of the membrane potential in the
313 time domain (see Methods). During the last second before the projected time to collision there was a
314 clear increase in the spectral density, but the highest signal power remained concentrated at 1-2 Hz
315 (Fig. 1F). During this period, spiking activity is highest (Fig. 1C) leading to a modest increase in
316 power at higher frequencies (Fig. 1F, gray box). That the signal power of the LGMD membrane
317 potential is highest at low frequencies despite the high frequency of synaptic inputs could be due to the
318 activation characteristics of these inputs or to the LGMD's membrane implementing a low-pass filter
319 favoring low frequency signals. We tested the latter possibility by measuring the frequency-resolved
320 input and transfer impedance of the LGMD's membrane. The input impedance reveals the mapping of
321 synaptic current frequencies to local dendritic membrane potential ones, while the transfer impedance

322 documents the change in membrane potential frequency content as the signal propagates from the
323 dendrites toward the SIZ.
324 **Single and dual dendritic LGMD recordings in vivo in response to chirp currents.** The LGMD's
325 input and transfer impedance were measured by recording *in vivo* the membrane potential with sharp
326 electrodes (Fig. 2A). These experiments consisted of injecting chirp currents during single or paired
327 recordings in the excitatory dendritic field. A chirp current is a sine waveform with time-varying
328 frequency; in the present recordings all chirps consisted of monotonically increasing frequency
329 sweeps. With each recording electrode we simultaneously measured the current and potential, allowing
330 us to calculate the gain and phase of the current-voltage transfer. The gain and the phase of this
331 transform are encapsulated in the complex-valued, frequency dependent membrane impedance *Z(f)*.
332 Further, by superposing chirp currents on different DC holding currents allowed us to measure
333 impedance at multiple steady-state membrane potentials (V_{ss}; Fig. 2B), and thus at different steady-
334 state activation levels of subthreshold conductances present in the LGMD membrane. In general, chirp
335 responses looked consistent across V_{ss} values and tapered slightly with increasing frequency.
336 Examination of different periods of the chirp show that at low frequencies the oscillations in
337 membrane current and potential were synchronous, while at higher frequencies the membrane potential
338 lagged behind the current and the change in potential was smaller (Fig. 2C). We conducted similar
339 experiments in voltage clamp and found similar changes to occur (Fig. 2D).
340 Quantification of transfer impedance characteristics was made as a function of the distance
341 between different pairs of dendritic recordings. The inter-electrode distance was measured both as the
342 dendritic path length between the electrodes in experimental micrographs (path distance, Fig. 2A), and
343 as the difference in back propagating action potential (bAP) amplitudes (electrotonic distance). At the
344 base of the excitatory dendritic field, the bAP amplitude was ~40 mV and decayed to <10 mV in distal
345 dendritic branches. The recording locations in the present study were primarily in larger branches with
346 bAP amplitudes between 20 and 40 mV. The path distances between these electrode pairs ranged from

347 63 to 150 µm. The difference in bAP amplitudes was well correlated with changes in membrane
348 potential transfer properties (Fig. 2E). In contrast, there was no correlation between path distance and
349 voltage attenuation ($r(9) = 0.17$, $p = 0.63$, Pearson linear correlation), likely due to differences in
350 dendrite diameter or number of branch points between the recording pairs. With increased electrotonic
351 distance between recording pairs, there was reduced voltage transfer and an increased delay. The
352 electrotonically closest recordings had ≤10% voltage attenuation, while for more distant pairs this
353 value increased to almost 50% (Fig. 2E). The average phase and time lags between locations was ~3°
354 and 0.5 ms between the most synchronous pairs and ~10° and 2 ms between the most asynchronous
355 pairs. For subsequent analyses of transfer impedance, data from all recording pairs were pooled.
356 **Impedance amplitude was consistent across holding potentials and chirp frequencies.** The
357 impedance amplitude is the absolute value of the complex impedance and represents the gain function
358 mapping at each frequency a given synaptic or electrode current into a change in membrane potential.
359 We measured the impedance amplitude at different V_{ss} values and examined how its profile changed
360 with holding potential. The LGMD dendrites have a resting membrane potential near -65 mV, can be
361 hyperpolarized by inhibitory inputs to below -70 mV, and are depolarized by excitatory inputs to >-50
362 mV during looming stimuli (Fig. 1C). We thus used V_{ss} values spanning that range, and confined
363 below the spike threshold potential.
364 Input impedance amplitude was highest at low membrane potentials (<-75 mV), particularly at
365 low frequencies (Fig. 3A, dashed box). Near the resting membrane potential, changes in V_{ss} produced
366 little change in impedance amplitude, despite the presence of HCN and M channels that have been
367 associated with membrane resonance in several cell types (Fig. 3A, red and yellow traces). Unlike
368 other HCN and M channel-expressing neurons that exhibit a pronounced resonant frequency, the
369 LGMD exhibited a more consistent input impedance amplitude profile (Gutfreund et al., 1995a;
370 Hutcheon et al., 1996; Hu et al., 2002; Gastrein et al., 2011). The transfer impedance amplitude
371 similarly changed little with membrane potential and tapered only slightly with increased frequency

372 (Fig. 3B). Accordingly, the voltage attenuation between paired recordings also showed a high overlap
373 across holding potentials (Fig. 3C). The variability of the voltage attenuation between recording pairs
374 was higher though, due to the differences in electrotonic distance (Fig. 2E). Consistency in impedance
375 at different holding potentials requires consistency in membrane conductance. The LGMD has large
376 HCN and M conductances which increase with hyperpolarization and depolarization, respectively
377 (Dewell and Gabbiani, 2018a, 2018b). That the impedance amplitude remains nearly constant at
378 different V_{ss} values suggests a reciprocal relation between these conductances such that their total
379 conductance remains roughly constant across holding potentials, particularly near V_{rest}. This in turn
380 would increase the consistency of EPSP amplitudes. This idea was confirmed by injecting simulated
381 EPSP waveforms at the same V_{ss} values used to measure impedance, resulting in EPSP amplitudes that
382 were independent of V_{ss} ($r(89) = -0.05$, $p = 0.63$, 91 V_{ss} values from 16 recordings in 9 animals).
383 The resonance properties of an electrical circuit are characterized by its bandwidth and
384 resonance strength (the Q factor, Horowitz and Hill, 2015). However, neuronal membranes have more
385 complex impedance profiles that are not as easily characterized. The most commonly used measure of
386 neuronal resonance strength is the ratio of peak to steady-state impedance (Koch, 1984).
387 Unfortunately, this measure ignores other frequencies and particularly those above the peak frequency.
388 So, in addition to this standard measure (see below, Fig. 6B), we wanted an additional measure that
389 incorporated impedance at frequencies below and above the resonant frequency and thus we
390 characterized the variability of the impedance amplitude by its standard deviation across frequencies
391 normalized to the mean impedance amplitude, which we call the frequency variation (see Methods).
392 The frequency variation of LGMD's input impedance was 10-15% and decreased slightly with
393 membrane depolarization (Fig. 3D, black). Transfer impedance had a frequency variation of ~20% and
394 also decreased with depolarization (Fig. 3D, red). At V_{rest} and the depolarized potentials seen during a
395 looming stimulus, there was little frequency variation and no prominent lowpass filtering of input or
396 transfer potentials, ruling out the membrane impedance as the cause of the power spectrum

397 concentration at low frequencies (Fig. 1E,F). Instead, this suggests that the low frequency power is due
398 to the activation characteristics of the synaptic inputs during a looming stimulus.

399 To test what electrical components could produce the impedance amplitude properties of the
400 LGMD, we created an array of RC and RLC circuit models (Fig. 3 E, F). For both model types we
401 used a specific membrane capacitance (C_m) and conductance (G_m) yielding a time constant (τ_m) of 6.9
402 ms, close to that measured experimentally in the LGMD (Gabbiani and Krapp, 2006; Peron et al.,
403 2007; Dewell and Gabbiani, 2018a, 2018b). The RLC circuit contained, in addition to the parallel
404 conductance and capacitance, a series conductance and inductance (Fig. 3F). We varied the percentage
405 of G_m that was in series with the inductance and the inductance time constant (τ_L) to determine which,
406 if any, parameters reproduced the LGMD's impedance amplitude. For most of the tested parameter
407 space, the circuit model's input impedance amplitude varied more with frequency than that of the
408 LGMD (Fig. 3G). Circuits with a fast inductance (≤ 10 ms) had impedance amplitudes as consistent as
409 that of the LGMD, while slow inductances increased the frequency variation beyond that of an RC
410 circuit, which was already higher than that of the LGMD. This is surprising considering that the
411 LGMD's resting membrane conductance is heavily dependent on rectifying HCN channels with a time
412 constant of ~1 s (Dewell and Gabbiani, 2018a). To assess the importance of the LGMD's membrane
413 time constant to the frequency variation, we examined the same range of inductance values in an RLC
414 circuit with doubled τ_m (increasing τ_m by increasing C_m or by decreasing G_m had the same effect). With
415 the higher τ_m, no inductance parameters produced a frequency variation as low as that of the LGMD.
416 Therefore, the low frequency variation of the LGMD's impedance profile depends on a fast τ_L in
417 addition to the fast τ_m. Of the LGMD's known conductances, g_M is a likely candidate to provide such a
418 fast inductance.

419 **Impedance phase reveals high membrane synchrony consistent across holding potentials.** Here
420 we refer to a neuron's membrane synchrony as the extent to which changes in membrane potential are
421 in phase with input currents of different frequencies. Membrane capacitance produces a phase lag

422 between input currents and their resulting change in membrane potential that increases both with
423 frequency and distance of propagation. Conductances like g_H and g_M counteract this delay and increase
424 the synchrony between synaptic input currents and the membrane potential (Ulrich, 2002; Narayanan
425 and Johnston, 2008; Hu et al., 2009; Vaidya and Johnston, 2013). To characterize the relative
426 synchrony of the LGMD's membrane potential with respect to current inputs, we thus measured the
427 frequency-dependent dendritic impedance phase. In a passive, isopotential neuron, membrane
428 capacitance forces input impedance phase to saturate at -90° as input current frequency increases
429 (Mauro, 1961; Narayanan and Johnston, 2008). Conversely, a positive impedance phase indicates that
430 the change in voltage precedes the change in current, a feature requiring a physiological process that
431 resembles an electrical inductance. Like impedance amplitude, the LGMD's impedance phase varied
432 little with V_{ss} values, distinguishing it again from other neurons where impedance phase has been
433 studied (Gutfreund et al., 1995a; Narayanan and Johnston, 2008). For all holding potentials, the phase
434 was positive at low frequencies (≤ 1 Hz). Although phase decreased with frequency, it saturated well
435 above -90° and in some recordings even increased at frequencies > 20 Hz. This was the case for both
436 the input and the transfer impedance phase (Fig. 4A and B, respectively). At depolarized potentials,
437 there was an additional small increase in phase for theta frequencies (Fig. 4A, B purple lines). The
438 LGMD subthreshold membrane potential exhibited zero phase and hence was most synchronous at ~1
439 Hz, in contrast to spiking which is most synchronous at 6 Hz (Dewell & Gabbiani 2018b).
440 Plotting as in Fig. 4C the real and imaginary components of the input impedance, called
441 respectively resistance and reactance, illustrates both the low frequency inductive and the high
442 frequency capacitive properties of the input impedance phase (corresponding to positive and negative
443 reactance, respectively). Such impedance locus plots combine the information on the impedance
444 amplitude (Fig. 3A) and phase (Fig. 4A): for each point in a locus plot if one were to draw a line
445 segment from the origin to the point, the length of the segment would be equal to the impedance
446 amplitude and the angle relative to the x-axis is the impedance phase. Fig. 4C confirms that the input

447 reactance was consistent across V_{ss} values while the input resistance increased at hyperpolarized
448 potentials resulting in rightward shift of the curves as V_{ss} decreases. The impedance locus plot of the
449 transfer impedance reveals even less change across membrane potentials, with only a small increase in
450 transfer resistance at hyperpolarized potentials (Fig. 4D). The relative phase of the input and transfer
451 impedances is the membrane potential phase lag with larger values indicating increased transfer delay
452 (Fig. 4E). The phase lag between input and transfer phase was also consistent across V_{ss} values and
453 was negative at frequencies ≤ 1 Hz, indicating an inductive phase shift on the propagating membrane
454 potential. The low frequency inductive characteristics of both the input and transfer impedance reveal
455 the influence of a slow inductor, likely the slowly rectifying HCN conductance.

456 Signal frequencies with zero reactance (and therefore an impedance phase of zero) are
457 synchronous; the membrane potential changes in unison with the membrane current. To test how
458 synchronous the LGMD's membrane was across the full range of frequencies examined, we converted
459 from phase to time and calculated the mean absolute asynchrony. This yielded a mean asynchrony of
460 ~2 ms between the input current and membrane potential at the input location independent of V_{ss} (Fig.
461 4F, grey). The asynchrony of the transfer impedance was ~3 ms at V_{ss} near -80 mV and decreased with
462 depolarization (Fig. 4F, red). We similarly measured the asynchrony of the membrane potential
463 recorded at the two positions, which was ≤ 1 ms (Fig. 4F, brown). To test how this measured
464 asynchrony compared to that of an RLC circuit, we surveyed the same parameter range as depicted in
465 Figure 3. No inductance parameters generated a circuit as synchronous as the LGMD. Circuits with a
466 large and fast inductance generated the lowest input impedance asynchrony, but this was still > 3.5 ms
467 (Fig. 4G). Reproducing the LGMD's low frequency inductive phase (Fig. 4A,B) required an RLC
468 circuit model with a slow inductance ($\tau_L \approx 1$ s). Dashed black lines of the low frequency insets (Fig.
469 4A,B & D) were produced by inductance parameters marked by the black star in Fig. 4G. Although the
470 addition of a slow inductance to an RLC circuit reproduced the low frequency inductance of the
471 LGMD membrane, it increased the input and transfer asynchrony of the circuit model further from that

472 of an RC circuit (Fig. 4H). The asynchrony between the membrane potential recorded at the two
473 locations could be reproduced by either cable model (Fig. 4H, right). This shows that the LGMD must
474 have an additional synchronizing influence unaccounted for by the circuit model. Whether this
475 increased synchrony is explainable by the LGMD's active membrane conductances is not immediately
476 evident.

477 **HCN and M channels reduce impedance amplitude and frequency variation.** To assess the
478 influence of HCN and M channels on the LGMD's input impedance profile, we measured the input
479 impedance before and after addition of two channel specific blockers: ZD7288 and XE991,
480 respectively. Blocking g_H reduces the resting membrane potential and input resistance of the LGMD
481 (Dewell and Gabbiani, 2018a), so after HCN blockade with ZD7288 we applied chirps with lower
482 peak current and higher DC holding current to generate equivalent V_{ss} values and changes in
483 membrane potential (Fig. 5A). After g_H blockade a decrease in the membrane potential was seen with
484 increasing chirp frequencies. Examination of the impedance amplitude shows that low frequency
485 impedance doubled after g_H blockade and that the impedance decreased more steeply with input
486 frequency (Fig. 5B). A reduction in inductance was also clear from the decreased impedance phase
487 after g_H block (Fig. 5C).

488 Blockade of g_M with XE991 increases the LGMD's resting membrane potential and input
489 resistance (Dewell and Gabbiani, 2018b), so we used decreased holding currents and chirp amplitudes
490 after blockade to account for these changes. After g_M blockade, a resonance emerged (Fig. 5D,
491 arrowhead). This was reflected in the peak near 4 Hz in the impedance amplitude profile (Fig. 5E).
492 This increased 4 Hz impedance likely helps generate the increased spiking observed in response to ~4
493 Hz inputs following g_M blockade (Dewell & Gabbiani 2018b). After g_M blockade the impedance phase
494 increased at frequencies ≤ 2 Hz and decreased at higher frequencies (Fig. 5F). These effects suggest
495 that in addition to implementing an inductance evident above 2 Hz, g_M also counteracts an additional
496 inductance that increases impedance amplitude at frequencies around 4 Hz and phase at frequencies ≤

497 2 Hz. Both g_M and g_H reduced the frequency variation of the LGMD, with g_M causing a larger
498 reduction at depolarized potentials and g_H reducing it more at hyperpolarized potentials, consistent
499 with their activation kinetics (Fig. 5G). Finally, the impedance locus plots show that the increased
500 frequency variation after block of either channel is due to a large increase in the range of resistances
501 and a reduced high frequency reactance (Fig. 5H).

502 The resonant frequency of the LGMD increased with membrane potential in the control
503 condition but was more consistent across V_{ss} values after blockade of either g_H or g_M (Fig. 6A). The
504 strength of resonance was small at all V_{ss} values in control conditions and after g_H block (Fig. 6B).
505 After g_M block, though, at resting V_m and above a strong membrane resonance was observed with
506 impedance amplitudes around 3 Hz (Fig. 6A) double that of steady state (0 Hz) impedance (Fig. 6B).
507 Both conductances contribute to the low overall membrane impedance of the LGMD, with g_H causing
508 the largest reduction in maximum impedance amplitude at and below resting Vm and g_M reducing the
509 maximum impedance amplitude at depolarized potentials (Fig. 6C). After g_H block, this maximum
510 impedance occurred at ≤ 1 Hz for all membrane potentials (Fig. 6A). Although we did not measure the
511 effects of g_H and g_M blockade on transfer impedance, there was a high similarity between input and
512 transfer resonance in control conditions (transfer and input resonant frequencies were within 1 Hz of
513 each other and resonance strengths differed by < 0.05 for >75% of trials). So, the changes in transfer
514 resonance after channel block would most likely parallel the changes shown for input resonance.

515 In addition to reducing the impedance amplitude and making it more consistent across
516 frequencies, both g_H and g_M increased the membrane synchrony. After blockade of either channel the
517 input asynchrony increased, with g_M blockade having the largest effect (Fig. 6D). The large change in
518 synchrony after g_M blockade was due to a more capacitive minimum phase at high frequencies (Fig.
519 6E) and a more inductive maximum phase at low frequencies (Fig. 6F). This g_M dependent increase in
520 membrane synchrony could underlie the g_M dependent increase in spike timing precision observed
521 previously (Dewell & Gabbiani 2018b). Although, the range of impedance phases did not increase

522 significantly after g_H blockade, the input impedance phase decayed to a minimum at a lower frequency
523 (Fig. 5C). Both g_H and g_M improve the input synchrony of the LGMD, but even after blocking the
524 channels, the LGMD membrane was more synchronous than any RLC circuit model (compare Fig. 6D
525 and Fig. 4H). This suggests that there must be an additional mechanism beyond these membrane
526 conductances that increases the LGMD's membrane synchrony.

527 **Neuronal morphology increases membrane gain and high frequency synchrony.** To test the
528 influence of the LGMD's morphology on membrane impedance we conducted simulations with a
529 passive LGMD model. Plotting the input impedance phase of every section of the LGMD (Fig. 7A)
530 revealed that it was larger than that of an isopotential model (dashed line) indicating higher synchrony
531 between a local input current and membrane potential. For the same frequency range used in
532 experiments, the passive LGMD model segments had input asynchronies of 2.1 ± 1.1 ms, matching
533 experimental data (c.f. Fig. 4H). This suggests that the LGMD morphology plays a bigger role in the
534 membrane's input synchrony than its active conductances. The model showed a monotone decrease in
535 phase at frequencies below 35 Hz, but at higher frequencies the phase oscillated with a different
536 amplitude and period for each section (Fig. 7A). For all frequencies, all sections had higher input
537 synchrony than an isopotential equivalent model, with an average phase increase of ~60° for
538 frequencies ≥ 100 Hz (Fig. 7A, inset). The input impedance amplitude was also altered by cell
539 morphology, decreasing less with frequency than in an isopotential equivalent model (Fig. 7B; dashed
540 line). The input frequency variation of the model sections was 8.6 ± 4.7% for the physiologically
541 dominant frequency range (< 35 Hz; see Fig. 1), demonstrating that the LGMD's morphology alters the
542 input impedance amplitude profile as much as its active conductances. At higher frequencies, the input
543 impedance amplitude remained monotonically decreasing, but was always higher than that of the
544 isopotential model (Fig. 7B, dashed line). The largest average increase over that of the isopotential
545 model of 46% came at 210 Hz (Fig. 7D inset).

546 To determine whether the effects of morphology on impedance was unique to the LGMD, we
547 conducted similar simulations using four other neuronal morphologies covering a range of sizes and
548 branching patterns (Fig. 7C). For all morphologies, input impedance increased relative to their
549 isopotential equivalents (otherwise identical model but with zero axial resistance), with largest average
550 increase in the LGMD and a cerebellar Purkinje model for both the phase and amplitude (Fig. 7D and
551 E). Models of layer 2/3 pyramidal, CA1 pyramidal, and oriens-lacunosum moleculare (OLM) neurons
552 had a progressively smaller increase in input impedance relative to their isopotential equivalents (Fig.
553 7D,E).

554 Hence, the branched structures of the LGMD and other neurons enhance local inputs with
555 increased gain and higher synchrony, although this was offset in part by lower signal transfer because
556 the branching and axial resistance also increase voltage attenuation between cell regions. The net effect
557 of the morphology on the membrane impedance is therefore not immediately apparent. In experiments,
558 transfer impedance was measured by injecting current at a single location and recording the membrane
559 potential at another. Synaptic currents, however, impinge at thousands of locations spread out across
560 the dendrites. Furthermore, these inputs don't propagate independently to the site of spike initiation.

561 To assess the net effect of morphology on impedance we thus calculated the transfer impedance
562 in an all-to-all manner, with current frequencies between 0 and 5 kHz injected into each model
563 segment and the impedance measured in all other segments of the model. An example of transfer
564 impedance profiles from one dendritic segment of the LGMD is illustrated for a 35 Hz current in Fig.
565 7F (amplitude on left, phase on right). These plots show that segments near the current injection site
566 (arrowheads) had higher transfer impedance while more distant segments had lower transfer
567 impedance than an isopotential equivalent (dashed lines). For all segments of all models, at all
568 frequencies, nearby segments exhibited increased and distant segments decreased transfer impedance
569 relative to the isopotential model. To determine how far signals propagated before the increased
570 attenuation overcame the increased input impedance, we quantified, for each segment, its area of

increased transfer impedance relative to an isopotential equivalent. This was recorded as a percentage of membrane for which transfer amplitude and phase were increased compared to the equivalent isopotential model. In Fig. 7F, this percentage would correspond to the surface area of the segments marked in red divided by the total membrane area (red and black).

For currents injected into some LGMD segments, the surface area with increased transfer amplitude was as high as 90% and amounted to ~70% for the average segment (Fig. 7G, black). The Purkinje model had a similar area of increased transfer as the LGMD (Fig. 7G, purple). Models of the pyramidal and OLM neurons, however, had an increased transfer amplitude from most segments to ~90% of the neuron's surface area (Fig. 7G). These observations do not match those on input impedance amplitude (Fig. 7D), suggesting that the LGMD and Purkinje morphologies are more compartmentalized, with a higher (local) input impedance amplitude increase but a lower increase of transfer impedance amplitude.

Across models, the increased input phase transferred to less of the cells' surface, though (Fig. 7H). For the LGMD, the improved synchrony of the input impedance spread throughout most of the neuron. At best, transfer from some segments retained a more synchronous phase to 90% of the LGMD surface, and on average inputs had higher transfer phase than in a corresponding isopotential model to 67% of the neuron (Fig. 7H, black). The Purkinje neuron had improved transfer phase to a slightly smaller portion of the neuron, with transfer from the average segment retaining improved synchrony to 57% of the neuron (Fig. 7H, purple). The average model segment of pyramidal neurons and the OLM interneuron had improved transfer phase to slightly less than 50% of the rest of the neuron (Fig. 7H). That the morphologies with a larger area of increased transfer amplitude had smaller areas of increased transfer phase indicates a tradeoff between timing and gain in the neuronal morphology with the LGMD and Purkinje morphologies providing more sensitive temporal discrimination of inputs and the pyramidal and interneuron morphologies providing increased signal gain.

In addition to quantifying the area of improved transfer, we also calculated membrane area weighted averages of the transfer to examine the net effect of the morphology on signal transfer. As neuronal branched morphologies cause membrane potentials to attenuate and increase delays, it would not be surprising if the net effect of the branching morphology were a reduced transfer amplitude (and synchrony, see next paragraph) relative to an isopotential model. This was not the case. The average transfer impedance amplitude for the morphologies tested were all slightly increased above their isopotential equivalent (Fig. 7I, dashed line). Each morphology generated a small bandpass increase in transfer amplitude (Fig. 7J). The CA1 pyramidal model had the highest increase, with 40 Hz inputs having a net increase of 9%. The LGMD and Purkinje morphologies generated smaller, higher frequency peaks of 4-5% increase near 65 Hz. This shows that the branching morphology of neurons provide a bandpass increase to the overall membrane gain.

To calculate the average transfer phase, values were weighted by the strength of the transfer amplitude: if there is minimal signal transfer between 2 segments then the phase of that transfer is less relevant. All morphologies had increased net transfer phase for signals above 100 Hz (Fig. 7K, L). For lower frequencies, the increased input synchrony was almost exactly counteracted by transfer delay yielding almost no net effect of morphology on low frequency phase (Fig. 7L, inset). The overall effect of the morphologies on transfer phase was minimal on low frequency signals, but improved the synchrony of high frequency signals, like those generated from fast synaptic currents.

Discussion

Here we have described the impedance properties of the LGMD *in vivo*, measured over the range of frequencies encompassing most of the signal power mediated by the LGMD's synaptic inputs. We found that the membrane impedance amplitude of the LGMD is consistent over the range of subthreshold membrane potentials and input frequencies involved in the detection of approaching objects. Further, the membrane impedance revealed a high degree of synchrony between input current

620 and resulting changes in membrane potential. This membrane synchrony and gain consistency were
621 both increased by the conductances g_H and g_M, as well as the neuron's branching morphology.
622 Despite a high rate of spontaneous and stimulus-evoked synaptic inputs due to the large number
623 of excitatory synapses the LGMD receives (Rind et al., 2016), most of its membrane power was
624 concentrated at low frequencies (Fig. 1E). During looming stimuli, as the rate of excitation increased,
625 the dominant signal frequency actually decreased with over 50% of the membrane potential spectral
626 power below 1.5 Hz (Fig. 1E, F). As neither the input nor the transfer impedance amplitude of the
627 LGMD were lowpass (Fig. 3A, B), this must reflect the characteristics of pre-synaptic inputs to the
628 LGMD. Neither the membrane gain, nor its synchrony changed dramatically over the frequencies
629 tested, favoring integration over a broad frequency range during looming. Yet, close to rest the
630 membrane gain was highest at 1.8±2.8 Hz (Fig. 3A) and synchrony (zero phase) was highest at 1.3±1.0
631 Hz (Fig. 4A), well within the range of dominant frequencies during looming stimuli (Fig. 1F). These
632 properties likely help shape the LGMD's selectivity for looming stimuli. If the LGMD's membrane
633 were lowpass it would decrease its ability to discriminate transient signals. In escape behavior,
634 selectivity is as important as detection, and the LGMD reliably discriminates between stimuli that
635 generate different, transient, synaptic input patterns (Gray et al., 2001; Peron and Gabbiani, 2009;
636 Dewell and Gabbiani, 2018a). A more broadband membrane could thus help discriminate among
637 patterns of the synaptic inputs.
638 This raises the question of what shapes the frequency dependence of the membrane gain. We
639 found that the neuron's morphology (Fig. 7C) and the active conductances g_H and g_M (Fig. 5G)
640 dramatically reduced frequency variation of the membrane gain. This is surprising, as both g_H and g_M
641 increase as the membrane potential moves away from their reversal potential, thus providing negative
642 (restorative) feedback in response to membrane potential changes. Hence, g_H and g_M have been
643 categorized as 'inductive' making neurons more bandpass (Hutcheon and Yarom, 2000; Narayanan and
644 Johnston, 2008; Hu et al., 2009; Hönigsperger et al., 2015). Examination of the effect of g_H on the

645 membrane gain (Fig. 5B), reveals that its primary effect on the LGMD is in fact the same as in other
646 neurons, reduction of lowpass filtering. This will produce bandpass resonance, if the resulting highpass
647 inductance is strong enough, when paired with the lowpass effect of membrane capacitance. Therefore
648 whether the g_H narrows the membrane bandpass properties or broadens them, as it does here and in
649 CA3 interneurons (Anderson et al., 2011), depends on the relative balance of its effects and those of
650 other membrane properties.

651 That the overall influence of a conductance on membrane impedance is due to its interaction
652 with other membrane properties is even clearer in the effects seen when blocking g_M. In thalamic relay
653 neurons, low voltage activated Ca^{2+} (Ca_{LVA}) channels produce bursting and a 2-4 Hz resonance
654 (Hutcheon et al., 1994; Puil et al., 1994). The LGMD also has a Ca_{LVA} conductance that can generate
655 bursting (Peron and Gabbiani, 2009; Dewell and Gabbiani, 2018b). As recently shown, g_M antagonizes
656 this bursting, thus regulating the LGMD firing pattern (Dewell and Gabbiani, 2018b). Blockade of g_M
657 also generated a change in impedance amplitude resulting in a 2-5 Hz resonance (Fig. 5D) matching
658 the frequency range of LGMD calcium bursts following g_M block (Dewell and Gabbiani, 2018b). In
659 hippocampal pyramidal neurons g_M blockade does not result in resonance (Hu et al., 2002, 2009),
660 suggesting that g_M antagonism of a Ca_{LVA} conductance likely does not occur in these neurons. It would
661 be interesting to test whether the resonance mediated by Ca_{LVA} channels in relay thalamic neurons is
662 similarly regulated by g_M.

663 In addition to showing low frequency variation, the impedance of the LGMD also showed
664 consistency across membrane potentials. As an object approaches increasing excitation causes
665 dendritic depolarization of >20 mV, so changes in dendritic integration properties with membrane
666 potential would influence the detection of impending collisions. Neither the amplitude nor the phase of
667 the membrane impedance changed much from -70 to -55 mV (Fig. 3 and 4). This consistency can also
668 be largely explained by g_H and g_M. At hyperpolarized potentials g_H increases, dominating the
669 membrane conductance, while conversely g_M increases with depolarization. At the LGMD's resting

membrane potential (-65 mV), both channels have large conductances and shallow activation kinetics (Dewell and Gabbiani, 2018a, 2018b). This improves the consistency of the total membrane conductance with changing membrane potential. If the activation ranges of g_H and g_M had less overlap in the LGMD, they would be more likely to dominate within their activation range creating the separate hyperpolarized and depolarized resonances seen in pyramidal cells (Hu et al., 2002, 2009). This too demonstrates the importance of interactions between conductances in determining their effect on the membrane's integration properties. As both g_H and g_M have kinetics that are sensitive to numerous modulators, the channel interactions are likely dependent on modulatory state (Delmas and Brown, 2005; Wahl-Schott and Biel, 2009). An advantage of *in vivo* characterization, as done here, is that the channels are in their intrinsic modulatory state.

Synaptic integration is influenced by the membrane synchrony as well as its gain. Like for the gain we found LGMD synchrony to be consistent across membrane potentials (Fig. 4A, B). We also found that the LGMD membrane was more synchronous than could be explained by a circuit model (Fig. 4H). The synchrony was enhanced by both g_H and g_M (Fig. 6D-F). Blockade of g_M produced a capacitive phase shift at high frequencies and an inductive phase shift at low frequencies leading to reduced synchrony. The low frequency inductive shift is most likely through interactions with Ca_{LVA} channels (see above). In contrast, g_H had less influence on high frequencies but reduced low frequency synchrony. At 1.3 Hz which is near the peak membrane power during looming stimuli (Fig. 1F) g_H blockade increased the asynchrony from 0 to 10 ms.

Although g_H and g_M increased synchrony, the LGMD remained more synchronous after their blockade than an equivalent circuit model. Testing a morphologically realistic LGMD model revealed that the neuron's shape increased the membrane's input synchrony as much as the active conductances (Fig. 7A, B). The branching morphology introduces new electrical paths whose axial resistivity does not decrease with frequency. This led to increased input gain and input synchrony. Previous modeling of dendritic atrophy in pyramidal neurons and Purkinje branching morphology have also found

increased gain and phase due to dendritic branching (Dhupia et al., 2015; Ostojic et al., 2015). This led us to wonder how the influence of LGMD's morphology on impedance compared to other cell morphologies, and whether the increase in input impedance caused by an extended neuronal morphology was counteracted by decreased signal propagation. We tested this with transfer impedance simulations of five neuronal morphologies.

Transfer impedance is defined between two locations. While its technically infeasible to simultaneously record intracellularly from many places within a neuron, in a model it is no more difficult to measure transfer between one hundred locations than between two. The reason we chose to measure the all-to-all transfer rather than just transfer from individual dendrites to the site of spike initiation as usual is simple. In neurons, *in vivo* synaptic currents impinge throughout the dendrites and do not propagate in isolation, but continuously integrate with new inputs as they propagate. As far as we know, this is the first examination of the sum transfer of a dendritic arbor in this fashion, and it revealed that in the LGMD, as well as other cell morphologies, the net effect of the cell morphology is an increase in all-to-all impedance gain and high frequency synchrony. Additionally, we found that the net increase in gain is bandpass and provides a hitherto undescribed potential source of gamma resonance (30-100 Hz; Fig. 7I). This furthers previous findings on the effects of dendritic morphology on a neuron's integration capabilities (Moore et al., 1988; Mainen and Sejnowski, 1996; Dhupia et al., 2015).

Ultimately the desired integration properties of a neuron are dictated by the pattern of its inputs and its computational role. For hippocampal pyramidal neurons that receive theta rhythmic inputs, a strong theta (4-10 Hz) resonance and synchrony could be advantageous (Hutcheon and Yarom, 2000; Hu et al., 2009; Vaidya and Johnston, 2013). Similarly, it might be a computational benefit for cortical neurons to exhibit large impedance changes with membrane potential to enhance differences between up and down network states (Gutfreund et al., 1995b; Hasselmo, 2005; Heys et al., 2010; Wang, 2010). For auditory neurons, specialized in detecting high frequency sound waves, a low capacitance and fast

720 membrane lead to membrane resonance at frequencies up to 400 Hz (Remme et al., 2014; Mikiel-
721 Hunter et al., 2016). The LGMD detects approaching objects and discriminates their specific input
722 statistics from a wide range of other input patterns through their integration over a wide range of
723 membrane potentials. Thus, achieving a high consistency in membrane impedance across frequencies
724 and membrane potentials by a balance of active membrane conductances and an extended morphology
725 is exactly what is needed to fine tune escape behaviors.
726

727 **References:**

728 Anderson WD, Galván EJ, Mauna JC, Thiels E, Barrionuevo G (2011) Properties and functional
729 implications of I_h in hippocampal area CA3 interneurons. Pflügers Archiv - European Journal
730 of Physiology 462:895–912.

731 Barrow AJ, Wu SM (2009) Low-Conductance HCN1 Ion Channels Augment the Frequency Response
732 of Rod and Cone Photoreceptors. Journal of Neuroscience 29:5841–5853.

733 Buzsáki G, Moser EI (2013) Memory, navigation and theta rhythm in the hippocampal-entorhinal
734 system. Nature Neuroscience 16:130–138.

735 Cole KS (1941) Rectification and inductance in the squid giant axon. The Journal of General
736 Physiology 25:29–51.

737 Cuntz H, Borst A, Segev I (2007) Optimization principles of dendritic structure. Theoretical Biology
738 and Medical Modelling 4:21.

739 Das A, Rathour RK, Narayanan R (2017) Strings on a Violin: Location Dependence of Frequency
740 Tuning in Active Dendrites. Frontiers in Cellular Neuroscience 11 Available at:
741 http://journal.frontiersin.org/article/10.3389/fncel.2017.00072/full [Accessed June 4, 2018].

742 Delmas P, Brown DA (2005) Pathways modulating neural KCNQ/M (Kv7) potassium channels.
743 Nature Reviews Neuroscience 6:850–862.

744 Dewell RB, Gabbiani F (2018a) Biophysics of object segmentation in a collision-detecting neuron
745 Rieke F, ed. eLife 7:e34238.

746 Dewell RB, Gabbiani F (2018b) M current regulates firing mode and spike reliability in a collision
747 detecting neuron. J Neurophysiol in press.

748 Dhupia N, Rathour RK, Narayanan R (2015) Dendritic atrophy constricts functional maps in resonance
749 and impedance properties of hippocampal model neurons. Frontiers in Cellular Neuroscience 8
750 Available at: http://journal.frontiersin.org/article/10.3389/fncel.2014.00456/abstract [Accessed
751 June 4, 2018].

752 Eyal G, Verhoog MB, Testa-Silva G, Deitcher Y, Lodder JC, Benavides-Piccione R, Morales J,
753 DeFelipe J, de Kock CP, Mansvelder HD, Segev I (2016) Unique membrane properties and
754 enhanced signal processing in human neocortical neurons. eLife 5 Available at:
755 https://elifesciences.org/articles/16553 [Accessed September 5, 2018].

756 Fotowat H, Harrison RR, Gabbiani F (2011) Multiplexing of Motor Information in the Discharge of a
757 Collision Detecting Neuron during Escape Behaviors. Neuron 69:147–158.

758 Gabbiani F, Krapp HG (2006) Spike-Frequency Adaptation and Intrinsic Properties of an Identified,
759 Looming-Sensitive Neuron. Journal of Neurophysiology 96:2951–2962.

760 Gabbiani F, Krapp HG, Koch C, Laurent G (2002) Multiplicative computation in a visual neuron
761 sensitive to looming. Nature 420:320–324.

762 Gabbiani F, Mo C, Laurent G (2001) Invariance of Angular Threshold Computation in a Wide-Field
763 Looming-Sensitive Neuron. J Neurosci 21:314.

764 Gastrein P, Campanac émilie, Gasselin C, Cudmore RH, Bialowas A, Carlier E, Fronzaroli-Molinieres
765 L, Ankri N, Debanne D (2011) The role of hyperpolarization-activated cationic current in
766 spike-time precision and intrinsic resonance in cortical neurons *in vitro*: I_h and neuronal timing.
767 The Journal of Physiology 589:3753–3773.

768 Gray JR, Robertson RM, Lee JK (2001) Activity of descending contralateral movement detector
769 neurons and collision avoidance behaviour in response to head-on visual stimuli in locusts.
770 Journal of Comparative Physiology A: Sensory, Neural, and Behavioral Physiology 187:115–
771 129.

772 Gutfreund Y, yarom Y, Segev I (1995a) Subthreshold oscillations and resonant frequency in guinea-
773 pig cortical neurons: physiology and modelling. The Journal of Physiology 483:621–640.

774 Gutfreund Y, Yarom Y, Segev I (1995b) Subthreshold oscillations and resonant frequency in guinea-
775 pig cortical neurons: physiology and modelling. The Journal of Physiology 483:621–640.

776 Hasselmo ME (2005) What is the function of hippocampal theta rhythm?—Linking behavioral data to
777 phasic properties of field potential and unit recording data. Hippocampus 15:936–949.

778 Häusser M, Mel B (2003) Dendrites: bug or feature? Current Opinion in Neurobiology 13:372–383.

779 Heys JG, Giocomo LM, Hasselmo ME (2010) Cholinergic Modulation of the Resonance Properties of
780 Stellate Cells in Layer II of Medial Entorhinal Cortex. Journal of Neurophysiology 104:258–
781 270.

Hönigsperger C, Marosi M, Murphy R, Storm JF (2015) Dorsoventral differences in Kv7/M-current and its impact on resonance, temporal summation and excitability in rat hippocampal pyramidal cells: Kv7/M-channel differences in dorsal and ventral CA1 pyramidal cells. The Journal of Physiology 593:1551–1580.

Horowitz P, Hill W (2015) The Art of Electronics. The Art of Electronics, by Paul Horowitz, Winfield Hill, Cambridge, UK: Cambridge University Press, 2015.

Hu H, Vervaeke K, Graham LJ, Storm JF (2009) Complementary Theta Resonance Filtering by Two Spatially Segregated Mechanisms in CA1 Hippocampal Pyramidal Neurons. Journal of Neuroscience 29:14472–14483.

Hu H, Vervaeke K, Storm JF (2002) Two forms of electrical resonance at theta frequencies, generated by M-current, h-current and persistent Na^+ current in rat hippocampal pyramidal cells. The Journal of Physiology 545:783–805.

Hutcheon B, Miura RM, Puil E (1996) Subthreshold membrane resonance in neocortical neurons. Journal of Neurophysiology 76:683–697.

Hutcheon B, Miura RM, Yarom Y, Puil E (1994) Low-threshold calcium current and resonance in thalamic neurons: a model of frequency preference. Journal of Neurophysiology 71:583–594.

Hutcheon B, Yarom Y (2000) Resonance, oscillation and the intrinsic frequency preferences of neurons. Trends in Neurosciences 23:216–222.

Jones PW, Gabbiani F (2010) Synchronized Neural Input Shapes Stimulus Selectivity in a Collision-Detecting Neuron. Current Biology 20:2052–2057.

802 Jones PW, Gabbiani F (2012) Impact of neural noise on a sensory-motor pathway signaling impending
803 collision. Journal of Neurophysiology 107:1067–1079.

804 Koch C (1984) Cable theory in neurons with active, linearized membranes. Biological Cybernetics
805 50:15–33.

806 Lampl I, Yarom Y (1997) Subthreshold oscillations and resonant behavior: two manifestations of the
807 same mechanism. Neuroscience 78:325–341.

808 London M, Hausser M (2005) Dendritic Computation. Annual Reviews of Neuroscience 28:503–532.

809 Mainen ZF, Sejnowski TJ (1996) Influence of dendritic structure on firing pattern in model neocortical
810 neurons. Nature 382:363–366.

811 Mauro A (1961) Anomalous Impedance, A Phenomenological Property of Time-Variant Resistance.
812 Biophysical Journal 1:353–372.

813 Mauro A, Conti F, Dodge F, Schor R (1970) Subthreshold Behavior and Phenomenological Impedance
814 of the Squid Giant Axon. The Journal of General Physiology 55:497–523.

815 McMillan GA, Gray JR (2015) Burst Firing in a Motion-Sensitive Neural Pathway Correlates with
816 Expansion Properties of Looming Objects that Evoke Avoidance Behaviors. Frontiers in
817 Integrative Neuroscience 9 Available at:
818 http://journal.frontiersin.org/Article/10.3389/fnint.2015.00060/abstract [Accessed May 12,
819 2018].

820 Migliore M, Messineo L, Ferrante M (2004) Dendritic I_h Selectively Blocks Temporal Summation of
821 Unsynchronized Distal Inputs in CA1 Pyramidal Neurons. Journal of Computational
822 Neuroscience 16:5–13.

823 Mikiel-Hunter J, Kotak V, Rinzel J (2016) High-Frequency Resonance in the Gerbil Medial Superior
824 Olive Battaglia FP, ed. PLOS Computational Biology 12:e1005166.

825 Miyasho T, Takagi H, Suzuki H, Watanabe S, Inoue M, Kudo Y, Miyakawa H (2001) Low-threshold
826 potassium channels and a low-threshold calcium channel regulate Ca^{2+} spike firing in the
827 dendrites of cerebellar Purkinje neurons: a modeling study. Brain Research 891:106–115.

828 Moore LE, Yoshii K, Christensen BN (1988) Transfer impedances between different regions of
829 branched excitable cells. Journal of Neurophysiology 59:689–705.

830 Narayanan R, Johnston D (2008) The h Channel Mediates Location Dependence and Plasticity of
831 Intrinsic Phase Response in Rat Hippocampal Neurons. Journal of Neuroscience 28:5846–
832 5860.

833 O'Shea M, Williams JLD (1974) The anatomy and output connection of a locust visual interneurone;
834 the lobular giant movement detector (LGMD) neurone. Journal of Comparative Physiology
835 91:257–266.

836 Ostojic S, Szapiro G, Schwartz E, Barbour B, Brunel N, Hakim V (2015) Neuronal Morphology
837 Generates High-Frequency Firing Resonance. Journal of Neuroscience 35:7056–7068.

838 Peron S, Gabbiani F (2009) Spike frequency adaptation mediates looming stimulus selectivity in a
839 collision-detecting neuron. Nature Neuroscience 12:318–326.

840 Peron SP, Krapp HG, Gabbiani F (2007) Influence of Electrotonic Structure and Synaptic Mapping on
841 the Receptive Field Properties of a Collision-Detecting Neuron. Journal of Neurophysiology
842 97:159–177.

843 Peters HC, Hu H, Pongs O, Storm JF, Isbrandt D (2005) Conditional transgenic suppression of M
844 channels in mouse brain reveals functions in neuronal excitability, resonance and behavior.
845 Nature Neuroscience 8:51–60.

846 Puil E, Meiri H, Yarom Y (1994) Resonant behavior and frequency preferences of thalamic neurons.
847 Journal of Neurophysiology 71:575–582.

848 Remme MWH, Donato R, Mikiel-Hunter J, Ballestero JA, Foster S, Rinzel J, McAlpine D (2014)
849 Subthreshold resonance properties contribute to the efficient coding of auditory spatial cues.
850 Proceedings of the National Academy of Sciences 111:E2339–E2348.

851 Rind FC, Simmons PJ (1992) Orthopteran DCMD neuron: a reevaluation of responses to moving
852 objects. I. Selective responses to approaching objects. Journal of Neurophysiology 68:1654–
853 1666.

854 Rind FC, Wernitznig S, Pölt P, Zankel A, Gütl D, Sztarker J, Leitinger G (2016) Two identified
855 looming detectors in the locust: ubiquitous lateral connections among their inputs contribute to
856 selective responses to looming objects. Scientific Reports 6 Available at:
857 http://www.nature.com/articles/srep35525 [Accessed September 5, 2018].

858 Schlotterer GR (1977) Response of the locust descending movement detector neuron to rapidly
859 approaching and withdrawing visual stimuli. Canadian Journal of Zoology 55:1372–1376.

860 Sekulić V, Chen T-C, Lawrence JJ, Skinner FK (2015) Dendritic distributions of Ih channels in
861 experimentally-derived multi-compartment models of oriens-lacunosum/moleculare (O-LM)
862 hippocampal interneurons. Frontiers in Synaptic Neuroscience 7 Available at:
863 http://journal.frontiersin.org/Article/10.3389/fnsyn.2015.00002/abstract [Accessed September
864 5, 2018].

865 Ströhmann B, Schwarz DWF, Puil E (1995) Electrical Resonances in Central Auditory Neurons. Acta
866 Oto-Laryngologica 115:168–172.

867 Ulrich D (2002) Dendritic Resonance in Rat Neocortical Pyramidal Cells. Journal of Neurophysiology
868 87:2753–2759.

869 Ulrich D (2014) Subthreshold delta-frequency resonance in thalamic reticular neurons. European
870 Journal of Neuroscience 40:2600–2607.

871 Vaidya SP, Johnston D (2013) Temporal synchrony and gamma-to-theta power conversion in the
872 dendrites of CA1 pyramidal neurons. Nature Neuroscience 16:1812–1820.

873 Wahl-Schott C, Biel M (2009) HCN channels: Structure, cellular regulation and physiological
874 function. Cellular and Molecular Life Sciences 66:470–494.

875 Wang X-J (2010) Neurophysiological and Computational Principles of Cortical Rhythms in Cognition.
876 Physiological Reviews 90:1195–1268.

877 Zhu Y, Gabbiani F (2016) Fine and distributed subcellular retinotopy of excitatory inputs to the
878 dendritic tree of a collision-detecting neuron. Journal of Neurophysiology 115:3101–3112.

879

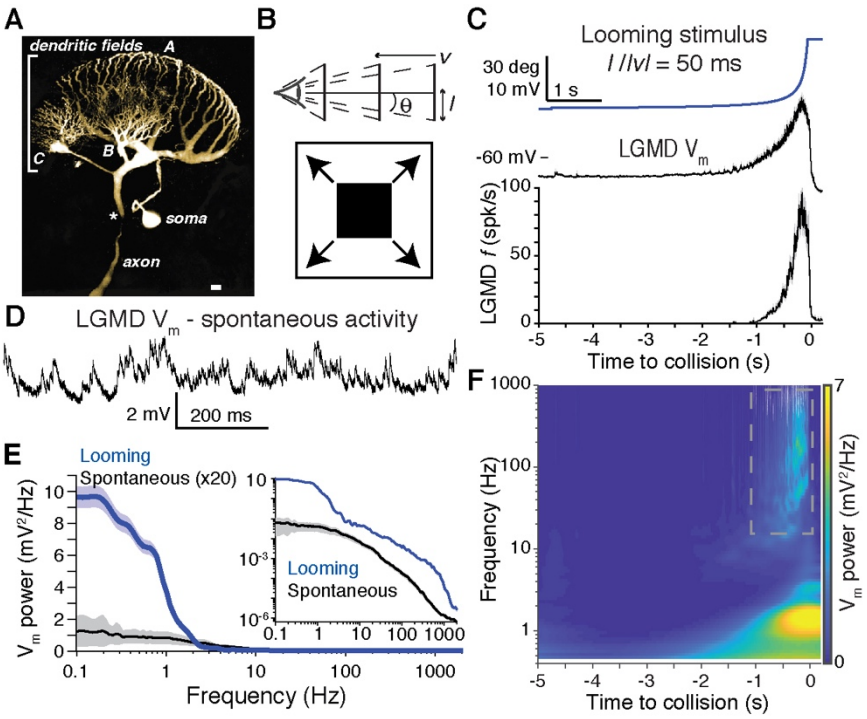

Dewell and Gabbiani, Fig. 1

Figure 1. Spontaneous and looming stimulus-evoked spectral power density of the LGMD's membrane potential. A) Micrograph of the LGMD, illustrating its dendritic fields (labeled A, B and C), the spike initiation zone (SIZ, marked with *) at the start of the axon, and the soma which lies outside of the neuron's electrical signal path (adapted from Gabbiani et al., 2002). Scale bar: 25 µm. B) A looming stimulus consists of a black square expanding symmetrically on the animal's retina (bottom). It simulates an object of half size l approaching on a collision course at constant velocity v (< 0), subtending an angular size θ(t) at the retina (top). C) Looming stimuli produce an angular size that increases nonlinearly over time (top, blue line). Most of the response to looming stimuli occurs shortly before the projected time of collision as can be seen in the average membrane potential (V_m, middle) and firing rate (bottom, displayed as mean ± standard error of the mean, sem, for 59 looming stimuli; N = 16 animals). D) Example recording of dendritic membrane potential within the LGMD while the eye was exposed to uniform illumination (V_m low-pass filtered at 10 kHz and digitized at 40 kHz). E) Despite the high frequency of spontaneous inputs, the V_m power is concentrated at frequencies below 5 Hz (black, abscissa is on logarithmic scale). During looming stimuli, the signal power increased 125-fold but remained concentrated at low frequencies (blue). Inset shows the data on a double logarithmic scale. Solid lines and shaded regions are mean ± sem (N=16 animals). F) Using wavelet analysis to measure the membrane potential power density in both the frequency and time domains reveals that during spiking there is increased high frequency power (dashed square), but the peak power remains at

899 frequencies <10 Hz. Plot displays the average power density map of the same 59 looming responses
900 shown in C and E.
901
902

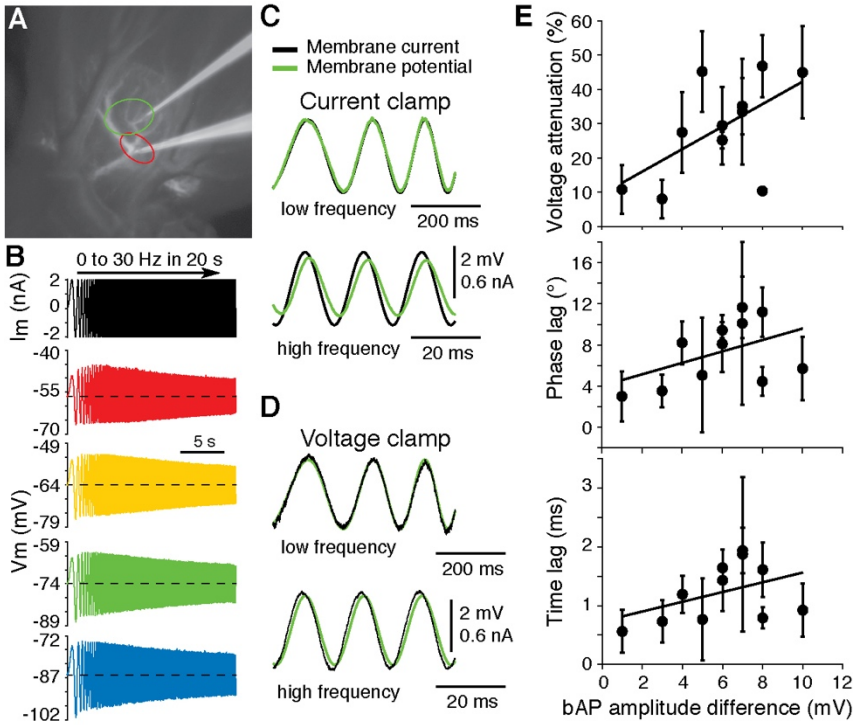

903 Dewell and Gabbiani, Fig. 2

904 **Figure 2.** Characterization of LGMD's membrane impedance profile with *in vivo* dendritic recordings.
905 A) Either single or dual recordings were made from dendritic field A and the primary neurite
906 connecting field A to the SIZ. Image taken with a CCD camera during a dual recording after staining
907 the LGMD with Alexa 594. The internal solution of both electrodes contained Alexa 594 for
908 visualization. Red and green ellipses encompass the region sampled by the proximal and distal
909 electrode, respectively, across 12 recording pairs (8 animals). B) To measure membrane impedance,
910 chirp currents (sine waveforms of increasing frequency) were injected at different steady-state
911 membrane potentials (V_{ss}). At top is an example of a linearly increasing chirp current followed by four
912 recordings of the membrane potential in response to this chirp current superposed on different holding
913 currents (I_{hold}). The values of I_{hold} and V_{ss} (dashed lines) were 2, 0, -2, -4 nA and -56, -64, -74, -86 mV,
914 respectively (from top to bottom). C) Examples traces of low and high frequency sections of the
915 measured membrane current and potential. At low frequencies the current and potential are
916 synchronous (~0° impedance phase) but at high frequencies the potential trails the current (negative
917 impedance phase). Note that at high frequencies the membrane potential is reduced relative to the

current indicating a reduction in impedance amplitude. D) Impedance measurements were similar when measured in voltage clamp. E) Signals attenuated more and had longer lags as the electrotonic distance increased between recording electrodes (estimated by the difference in amplitudes of the backpropagating action potential, bAP). Each point and error bar report the mean value and sd (across different V_{ss} values) for a recording pair (N = 11 recording pairs from 8 animals). Mean bAP amplitudes were 32 and 26 mV for the proximal and distal electrode; the dendritic path distance between recordings ranged from 63 to 149 µm with a mean of 105 µm.

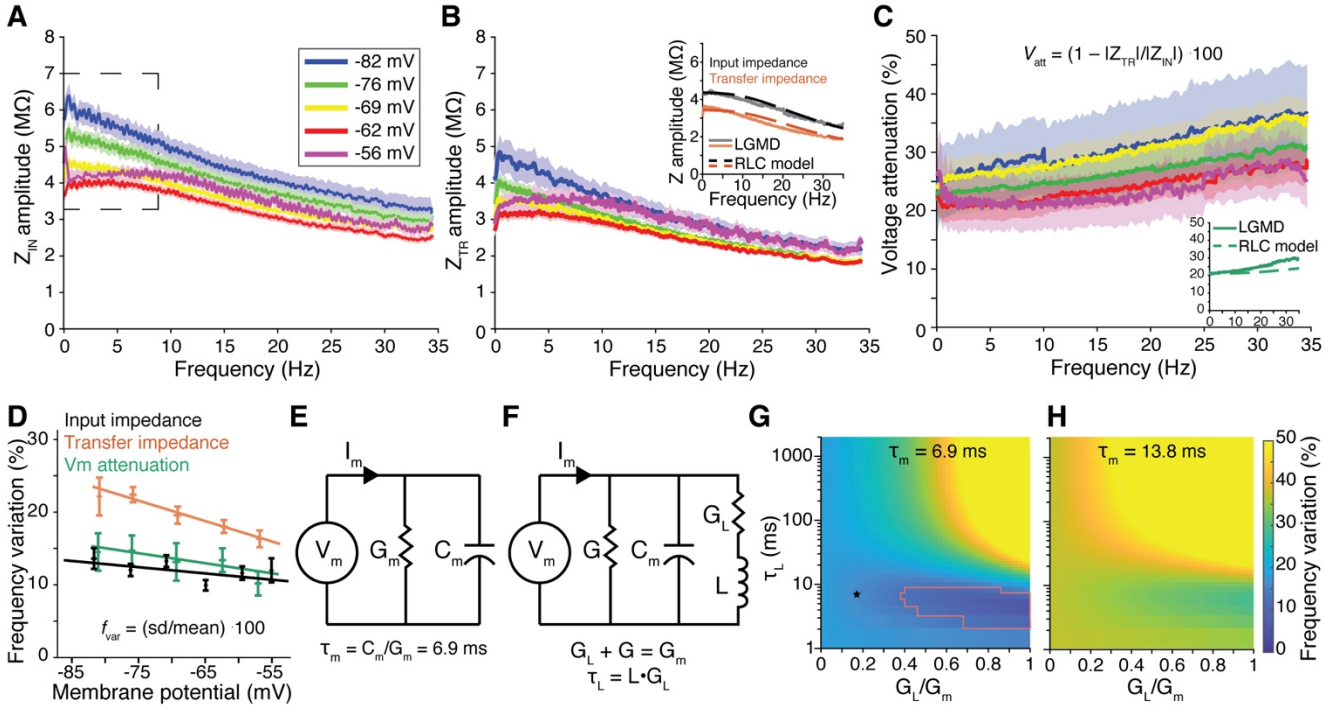

Dewell and Gabbiani, Fig. 3

Figure 3. The LGMD membrane impedance amplitude and voltage attenuation behave similarly across frequencies and membrane potentials. A) Input impedance (Z_{IN}) amplitude profiles measured at different steady-state membrane potentials (V_{ss}, see Fig. 2B) and displayed as mean ± sem (lines and shaded regions) reveal a high degree of overlap across membrane potentials. The lines only show clear separation for low frequencies (<10 Hz, dashed square) at membrane potentials >10 mV below V_{rest} (-65 mV). N = 76 recordings from 56 animals. B) The transfer impedance (Z_{TR}) amplitude between different dendritic sites also varied little across membrane potentials. The inset shows the average input and transfer impedance amplitudes (solid lines) overlaid with those of an RLC circuit model as depicted in panel F (dashed lines). N = 13 recording pairs from 10 animals. C) Voltage attenuation (V_{att}) is more variable between recordings than impedance amplitude (note the larger sem regions in C

when compared to A or B) with ~20–35% reduction in voltage between dendritic locations. The inset compares attenuation with that of the best-fit RLC model of panel F. Same data set as in B. D) The frequency variation (f_{var}) of the input and transfer impedance amplitude as well as that of voltage attenuation decreased slightly with membrane depolarization. The frequency variation shows the consistency across frequencies, with a value of 0 indicating an ideal resistor. E,F) RC and RLC circuits, respectively, were chained to obtain equivalent cylinder models for comparison with the data. For both circuit models G_m = 116 μS/cm^2 and C_m = 0.8 μF/cm^2. See methods for details on impedance calculations. G) Heatmap illustrating the effect of the RLC circuit inductor parameters on the frequency variation of its input impedance. The left edge (G_L = 0) corresponds to the RC circuit depicted in E. Slower inductor time constants (τ_L) increased frequency variation. Increasing the ratio G_L/G_m increased frequency variability for slow inductors and decreased it for fast inductors. The red line delimits the parameter region that had a frequency variation as low as the LGMD data. The star indicates the parameter values used for the insets in panels B and C which best matched the shape of the LGMD impedance amplitude profiles. H) Heatmap of an RLC circuit with τ_m twice that of the LGMD (increasing either C_m or decreasing G_m had the same effect). For this slower circuit model, no inductor parameter yielded an impedance as consistent across frequencies as the LGMD data. In G and H plotted values are for input impedance; transfer impedance maps look similar but with frequency variations of ~1.06 times those in the input impedance maps for all parameters.

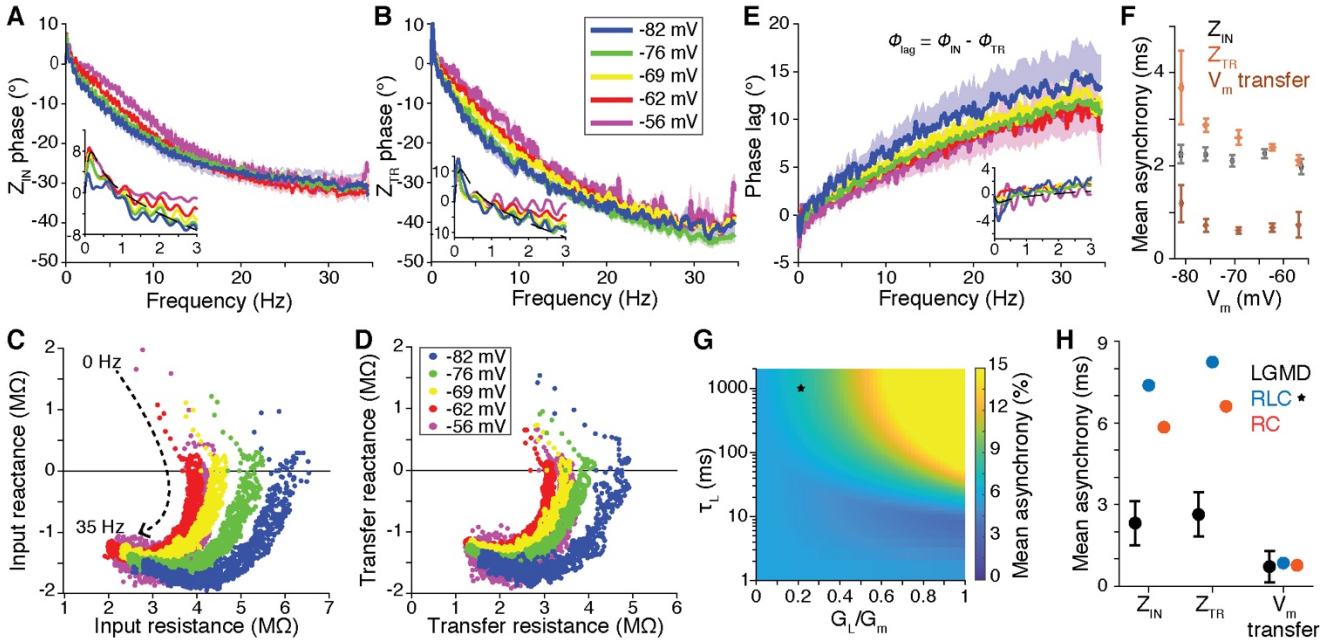

Dewell and Gabbiani, Fig. 4

959 **Figure 4.** LGMD membrane synchrony and consistency across membrane potentials. A) Z_{IN} phase
960 profiles (mean ± sem) are inductive (exhibit positive phase) only at frequencies < 1Hz (inset), show
961 high overlap across membrane potentials, and level off around -30°. N = 76 recordings from 56
962 animals. B) Z_{TR} phases similarly exhibit induction at frequencies < 1Hz (inset) and overlap across
963 membrane potentials. N = 13 recording pairs from 10 animals. C, D) Impedance locus plots show the
964 real (resistance) and imaginary (reactance) components of the impedance, pooled across frequencies
965 (dotted arrow). The membrane inductance at low frequencies is evidenced by the points with positive
966 reactance. At hyperpolarized potentials, resistance increased but otherwise the LGMD maintained a
967 consistent profile across membrane potentials. E) Phase lag of membrane potential at 'recording-only'
968 location relative to that at the 'recording and current injection' location. At frequencies <1 Hz there
969 was a phase advance with the more distant location preceding the input location (inset). The phase lag
970 increased steadily with frequency. F) Asynchrony was measured as the mean absolute time lag between
971 pairs of simultaneously recorded variables (0 ms equals perfect synchrony). Z_{IN} asynchrony
972 corresponds to the lag between the input current and local membrane potential. Z_{TR} asynchrony was
973 calculated from the lag between the input current and membrane potential at the secondary recording
974 location and V_m transfer asynchrony from the lag between the membrane potentials at the two
975 recording locations. Z_{TR} asynchrony decreased with membrane depolarization. G) RLC circuit input
976 asynchrony as a function of its inductor parameters. Z_{TR} asynchrony was ~1.1 times higher than Z_{IN}
977 values shown. The LGMD low frequency inductive phase could only be reproduced by a slow
978 inductor. Dashed black lines in insets of A, B and E produced by parameters marked by black star in G.
979 H) The LGMD exhibited higher synchrony between membrane current and voltage (phase nearer 0°)
980 than an RC circuit model ($G_L = 0$) or the RLC circuit model marked by black star in G. No RLC
981 parameters produce as small a mean Z_{IN} or Z_{TR} asynchrony as the LGMD.
982

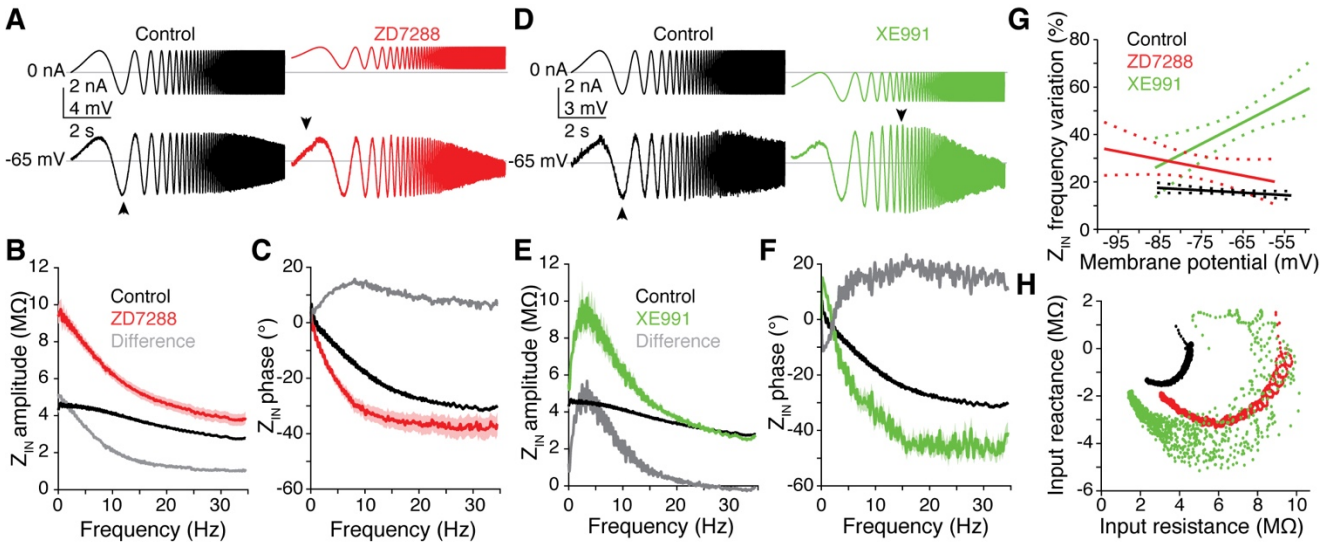

Dewell and Gabbiani, Fig. 5

Figure 5. Blockade of either HCN or M channels decreased membrane current-voltage synchrony and increased impedance variation with stimulus frequency. A) Example chirp currents (top) and membrane potential responses (bottom) before (left, black) and after (right, red) ZD7288 application. After drug application the chirp amplitude was decreased and I_{hold} was increased to produce a similar V_{ss} and similar changes in membrane potential. B) After blocking HCN channels with ZD7288, input impedance increased 2-fold at low frequencies. Population average impedance (across animals and V_{ss}) is shown as mean ± sem (solid line and shaded region). The grey line is the difference between the averages. C) Impedance phase decreased at all frequencies after HCN blockade, reducing membrane current-voltage synchrony. D) Example chirp currents (top) and response (bottom) before (left) and after (right) XE991 application. After drug application the chirp amplitude and I_{hold} were decreased to produce a similar V_{ss} and similar changes in membrane potential. E) After blocking M channels with XE991 a large increase in low frequency input impedance was also seen with peak at ~4 Hz. F) After M channel block impedance phase increased at low frequencies (<2 Hz) but decreased at higher frequencies. G) The increased low frequency impedance after blockade of HCN or M channels produced higher Z_{IN} frequency variations across steady-state membrane potentials. Z_{IN} frequency variation is displayed as linear fit (solid lines) and 95% confidence intervals (dotted lines). M channel blockade increased variation mainly at depolarized potentials while HCN blockade had a greater effect at hyperpolarized potentials. H) Input impedance locus plots before and after channel block show clear increases in both the resistance and capacitive reactance. Control data from 53 recordings at 181 V_{ss} from 44 animals; ZD7288 data includes 9 recordings at 36 V_{ss} from 6 animals; XE991 data includes 6 recordings at 14 V_{ss} from 6 animals.

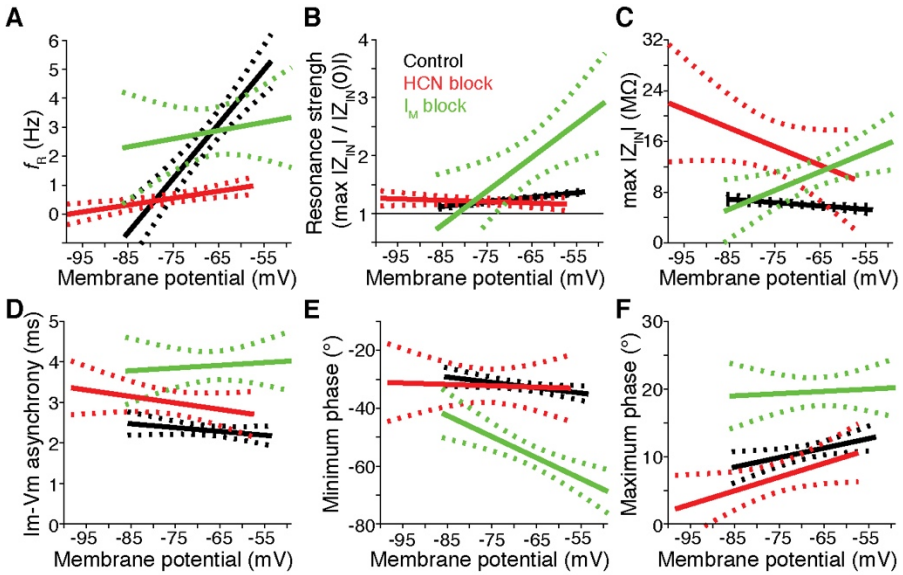

Dewell and Gabbiani, Fig. 6

Figure 6. Membrane resonance decreased after HCN block but increased after M channel block. A) The resonant frequency (f_R) of the LGMD increased with membrane potential under control conditions (black), but after HCN block f_R decreased to < 1Hz for all potentials (red). Following I_M block, f_R remained roughly constant at ~3Hz for all potentials (green). Data is plotted as best linear fit (solid line) and 95% confidence intervals (dashed lines). B) The resonance strength, calculated as the maximum impedance amplitude divided by steady-state impedance amplitude ($|Z_{IN}(0)|$), was <1.2 for all membrane potentials under control conditions and after HCN block. After I_M block, however, a larger resonance was observed at depolarized membrane potentials. C) Despite larger variations of the f_R with membrane potential under control conditions (see A), the maximum impedance amplitude (max $|Z_{IN}|$) changed more with V_m after either HCN or I_M blockade and was higher at all Vm values after HCN block and at depolarized Vm after I_M block. D) Input asynchrony measured as the mean absolute time lag between the input current and local membrane potential. I_m-V_m synchrony decreased by ~1 ms after HCN block (red) and ~2 ms after M channel block (green). Control data (black) is the same as shown in Fig. 4F. E) The minimum impedance phase reached at high frequency decreased after I_M blockade, especially at depolarized membrane potentials, approaching the -90° minimum phase of an isopotential circuit. F) Conversely, the peak impedance phase at low frequency increased after I_M block. Same recordings as in Fig. 5: control data from 53 recordings at 181 V_{ss} from 44 animals; ZD7288 data includes 9 recordings at 36 V_{ss} from 6 animals; XE991 data includes 6 recordings at 14 V_{ss} from 6 animals.

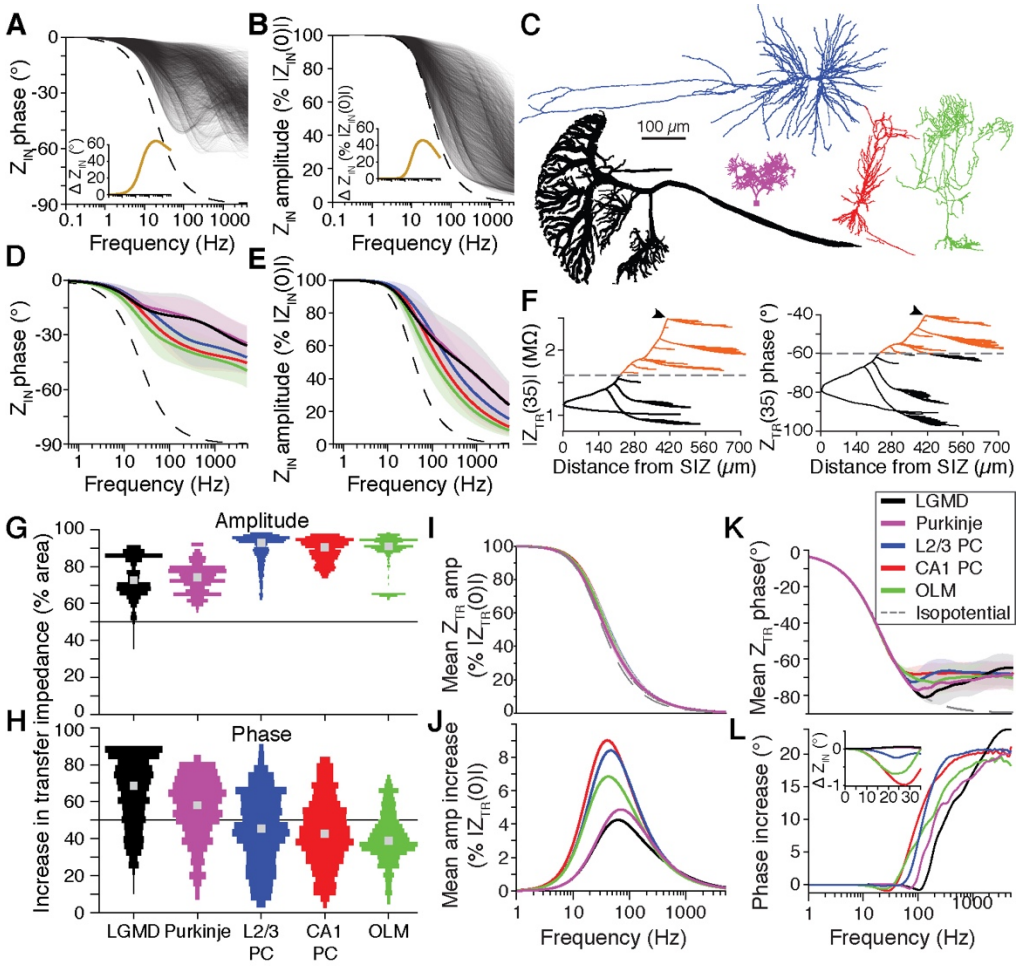

Dewell and Gabbiani, Fig. 7

Figure 7. Simulations of passive neurons reveal the influence of morphology on impedance characteristics. A) Every segment of the LGMD model (thin black lines) had higher input impedance phase than an isopotential model (dashed line). At frequencies >30 Hz input impedance phase oscillated, with a period and amplitude depending on the considered dendritic section. B) All sections of the LGMD model (thin black lines) exhibited a decrease in input impedance amplitude smaller than that of an isopotential model (dashed line). For each section the impedance amplitude is normalized to impedance at 0 Hz ($|Z_{IN}(0)|$). The difference between the input impedance amplitude and that of an isopotential model was maximal at ~200 Hz. Insets in A and B show the average difference between the extended and isopotential models. C) The effect of neuronal morphology on impedance was tested in the LGMD (black) and 4 other cell morphologies of different size and shape: a cerebellar Purkinje cell (purple), a hippocampal CA1 pyramidal cell (red), a cortical layer 2/3 pyramidal cell (blue), and a CA1 oriens lacunosum-moleculare interneuron (OLM; green). D) All neuron models tested had large increase in input phase compared to an isopotential equivalent model, with the LGMD and Purkinje models exhibiting the highest phase. Data is color coded to depictions in C and presented as mean ± sd

(solid lines and shaded regions). E) All morphologies had increased input impedance amplitude relative to their isopotential equivalents. Data presented as in D. F) Data from example dendritic segments of the LGMD model shows that at 35 Hz the transfer impedance amplitude (left) and phase (right) decreased with distance from the site of current injection (arrowhead). Segments for which transfer impedance was higher than that of an isopotential equivalent neuron (dashed line) are red. Data in G and H measured by summing the surface area of red segments and dividing by the total surface area. G) For each neuron model segment, we summed the surface area of other model segments for which signal transfer was increased compared to an isopotential equivalent and divided by the neuron's total surface area. Bar widths indicate how many model segments had improved transfer for each percentage range, and grey squares mark the average segment. All morphologies had increased transfer amplitudes compared to an isopotential equivalent model, with the LGMD and Purkinje morphologies having improved transfer for a smaller percentage of the neuron segments. H) For the LGMD and Purkinje morphologies most segments had improved transfer phase to the majority of the neuron (measured as sum area of segments with increased phase transfer over total area). For the other morphologies most segments had reduced transfer phase to other segments comprising the majority of the neuronal membrane. I) For all models, an average all-to-all transfer impedance was measured as a function of frequency (colored lines) and compared to the impedance of an isopotential equivalent (dashed line). All segments of all morphologies had very similar average transfer impedance profiles with only a small deviation from isopotential (dashed line; each model displayed as mean ±1 sd). J) The increase of each cell's mean transfer amplitude as a function of frequency from isopotential reveals a bandpass increase in average transfer gain. K) The average all-to-all transfer phase for each model was similar with improvements at frequencies above ~50 Hz relative to the isopotential model (dashed line); solid lines and shaded regions are mean ± 1 sd for each model. L) The average change in phase was slightly negative at frequencies near the cell's peak gain, and increased to ~20° in the kHz range. Inset shows the average effect on transfer phase over the physiologically dominant frequency range.